

Strong-Field Resonant Dynamics in Semiconductors

Michael S. Wismer,^{1,*} Stanislav Yu. Kruchinin,^{1,†} Marcelo Ciappina,¹
Mark I. Stockman,^{2,‡} and Vladislav S. Yakovlev^{1,2,§}

¹Max-Planck-Institut für Quantenoptik, Hans-Kopfermann-Straße 1, 85748 Garching, Germany

²Center for Nano-Optics (CeNO) and Department of Physics and Astronomy,
Georgia State University, Atlanta, Georgia 30340, USA

(Received 5 December 2015; revised manuscript received 1 March 2016; published 10 May 2016)

We predict that a direct band gap semiconductor (GaAs) resonantly excited by a strong ultrashort laser pulse exhibits a novel regime: kicked anharmonic Rabi oscillations. In this regime, Rabi oscillations are strongly coupled to intraband motion, and interband transitions mainly take place when electrons pass near the Brillouin zone center where electron populations undergo very rapid changes. The asymmetry of the residual population distribution induces an electric current controlled by the carrier-envelope phase of the driving pulse. The predicted effects are experimentally observable using photoemission and terahertz spectroscopies.

DOI: 10.1103/PhysRevLett.116.197401

The effect of strong electric fields on crystalline solids was long considered important as introduced by Zener [1] and developed by Keldysh [2]. Recently, a novel field studying the interaction of few-cycle high-intensity (with fields reaching or exceeding internal fields in the matter) optical pulses with solids has attracted a great deal of attention [3–12]. One of the most significant directions of the recent research was strong-field interaction of ultrashort pulses with transparent solids where the carrier frequency ω_0 and pulse bandwidth $\Delta\omega$ were well within the band gap: $\hbar\omega_0, \hbar\Delta\omega \ll E_g$, that is, the interaction was nonresonant. In this case, the characteristic response time τ_r is determined by the band gap: $\tau_r \gtrsim \hbar/E_g$ [6]. Consequently, light-induced processes are subcycle and depend on the carrier-envelope phase (CEP) [13].

Resonant ($\hbar\omega_0 \sim E_g$) interaction of intense ultrashort pulses with absorbing solids was also investigated. The CEP controllability of electron dynamics in this regime was mostly studied in the context of carrier-wave Rabi flopping (CWRP) [14–17], where the motion of charge carriers within bands was neglected. Also perturbative $\omega + 2\omega$ interference was investigated [18,19]. In this case, a relatively weak field limits the scope of the intraband motion.

Thus, in previously studied regimes, either intraband electron dynamics were important, or resonant light absorption played a dominant role. Here we consider a new strong-field regime where intraband dynamics fundamentally affect the resonant excitation. In this regime, transitions between bands occur within a small fraction of an optical cycle. Their quantum interference is predicted to cause a strong residual ballistic electric current that is controllable by the CEP.

We solve the length-gauge optical Bloch equations with intraband displacement terms [8,20]:

$$\frac{\partial}{\partial t}\rho_{ij} = \left[\frac{\delta_{ij} - 1}{T_2} + \frac{i}{\hbar}(E_i - E_j) \right] \rho_{ij} + \frac{1}{\hbar} \mathbf{F}(t) (e \nabla_{\mathbf{k}} \rho_{ij} - i [\hat{\mathbf{d}}, \hat{\rho}]_{ij}). \quad (1)$$

Here, $\rho(\mathbf{k}, t)$ is a density matrix, its diagonal elements, $n_i(\mathbf{k}, t) = \rho_{ii}(\mathbf{k}, t)$, are dimensionless probabilities to find an electron with crystal momentum \mathbf{k} in band i , T_2 is the dephasing time introduced phenomenologically, $e > 0$ is the elementary charge, and $d_{ij}(\mathbf{k}) = e \langle \psi_i(\mathbf{k}) | i \nabla_{\mathbf{k}} | \psi_j(\mathbf{k}) \rangle$ are dipole matrix elements that form matrix $\hat{\mathbf{d}}$. We obtained $d_{ij}(\mathbf{k})$ and the band energies $E_i(\mathbf{k})$ using the Wien2K code [21]. We assume that the electric field of the laser pulse in the medium $\mathbf{F}(t) \parallel \hat{\mathbf{e}}$ is linearly polarized along the $\Gamma - X$ direction in the Brillouin zone of GaAs, where the X point is at $k_{\max} = 1.11 \text{ \AA}^{-1}$. This choice eliminates second-order nonlinear effects, in particular, optical rectification [22]. We will denote the field projection on the $\Gamma - X$ direction as $F(t)$ and its amplitude as F_0 . The specific form of $F(t)$ is described in the Supplemental Material [23]. This is a 5 fs pulse with a central (carrier) photon energy of $\hbar\omega_0 = E_g = 1.55 \text{ eV}$.

Let us make a few estimates. Nondestructive measurements on GaAs with few-cycle pulses were reported for $F_0 = 0.4 \text{ V/\AA}$ (a peak intensity of $2 \times 10^{12} \text{ W/cm}^2$), where the onset of CWRP was observed [15,17]. This field is much smaller than that required to accelerate an electron from the Γ point ($\mathbf{k} = 0$) to the boundary of the Brillouin zone, which is $F_0 = 0.9 \text{ V/\AA}$ for $\hbar\omega_0 = 1.55 \text{ eV}$. Using $d = 5 e\text{\AA}$ [15] for transitions between the light-hole valence band (VB) and the lowest conduction band (CB), we estimate the ratio of the Rabi frequency $\Omega_R = dF_0/\hbar$ to the laser frequency as $\Omega_R/\omega_0 \approx F_0/(0.3 \text{ V/\AA})$. We also note that our laser pulse is much

shorter than the momentum relaxation time in GaAs, which is ~ 200 fs [33,34].

Figure 1 shows the residual current density,

$$j(F_0, \varphi_{\text{CE}}) = -\frac{2e}{(2\pi)^3} \sum_i \int_{\text{BZ}} d^3k n_i(\mathbf{k}, t_{\text{max}}) \hat{\mathbf{e}}v_i(\mathbf{k}), \quad (2)$$

for the cases of two [Figs. 1(a)–(c)] and six [Figs. 1(d)–(f)] bands, as well as for different values of T_2 . Using more than three conduction bands does not qualitatively change our results [23]. In Eq. (2), $v_i(\mathbf{k}) = \hbar^{-1} \nabla_{\mathbf{k}} E_i$ is the group velocity in band i , and $t_{\text{max}} = 36.2$ fs is the final time of our simulations. When the field is weak, the photocurrent is excited due to the $\omega + 2\omega$ interference [18,19]. In this case, it is known that $j_{\text{max}}(F_0) \propto F_0^3$ —cf. Fig. 2. This is due to

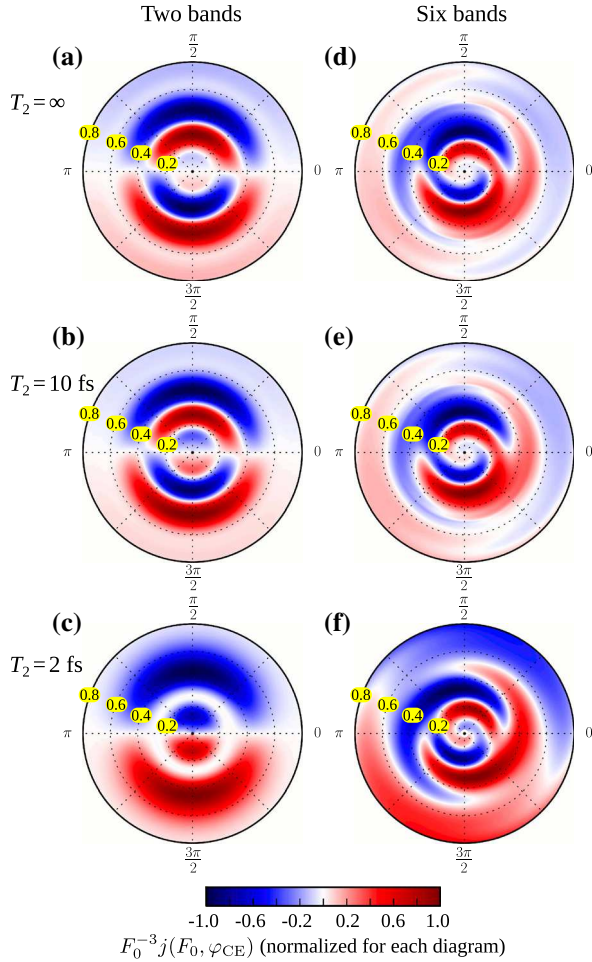


FIG. 1. The residual current density $j(F_0, \varphi_{\text{CE}})$. In these diagrams, the distance to the origin corresponds to the pulse amplitude F_0 , which varies from zero to 0.8 V/Å, while the angle to the horizontal axis encodes the carrier-envelope phase φ_{CE} . The color coding of $F_0^{-3}j(F_0, \varphi_{\text{CE}})$ is individually normalized for each diagram. Panels (a)–(c) show two-band results (1 VB, 1 CB), while panels (d)–(f) display outcomes of six-band (3 VBs, 3 CBs) calculations. Each horizontal pair of plots corresponds to a certain value of dephasing time T_2 as indicated by the labels.

the fact that the probability amplitudes of one- and two-photon processes are proportional to F_0 and F_0^2 , respectively, while their interference makes a contribution proportional to F_0^3 . In Fig. 2, this cubic dependence breaks down for $F_0 \gtrsim 0.1$ V/Å, which we visualize in Fig. 1 by representing $F_0^{-3}j(F_0, \varphi_{\text{CE}})$ with color coding. In Fig. 1, the results obtained for two and six bands differ significantly, which is consistent with recent findings [11]. However, they also share a few remarkable features.

First, we observe CEP-controlled light-induced residual current, which implies that it is due to ultrafast, subcycle processes. The cases of no polarization relaxation ($T_2 = \infty$) [panels (a) and (d)] and fast dephasing [$T_2 = 10$ fs, panels (b) and (e)] differ very little, which suggests that there is fast effective dephasing within the purely Hamiltonian system described by the Schrödinger equation. Note that the fastest electron dephasing time in semiconductors (GaAs) was measured to be $T_2 \sim 14$ fs [35], which was consistent with theory [36]. At the same time, recent experiments on high-harmonic generation in solids [8–12] suggest that dephasing times in the strong-field regime may be on the order of femtoseconds, so we also present results for $T_2 = 2$ fs. We note that T_2 has a stronger impact on the two-band results.

Second, for any chosen CEP, $j(F_0, \varphi_{\text{CE}})$ changes its sign at certain values of F_0 . In the two-band model, the maximum magnitude of the current at any field amplitude is always obtained for the antisymmetric pulse ($\varphi_{\text{CE}} = \pm\pi/2$). In contrast, for more realistic six-band calculations, the maximum current nontrivially depends on the CEP, which causes the appearance of “vortices” in panels (d)–(f).

Third, starting from $F_0 \sim 0.2$ V/Å, the residual current is much stronger than that obtained by extrapolating the weak-field current according to the $\propto F_0^3$ law. This fact is more clearly seen in Fig. 2, from which we also conclude that dephasing tends to reduce the magnitude of the residual current.

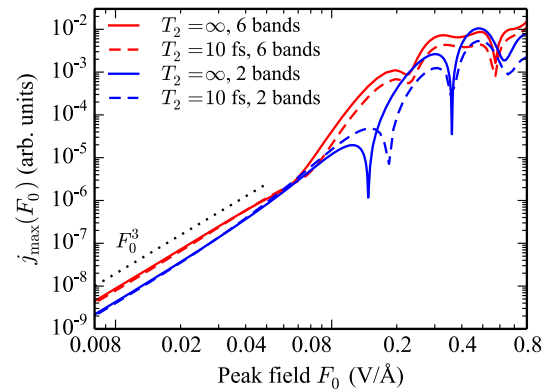


FIG. 2. The maximal value of the residual current density $j_{\text{max}}(F_0) = \max_{\varphi_{\text{CE}}} [j(F_0, \varphi_{\text{CE}})]$. The solid and dashed lines were obtained with $T_2 = \infty$ and $T_2 = 10$ fs, respectively. Red curves represent six-band calculations (3 VBs, 3 CBs), whereas blue curves show the two-band results (1 VB, 1 CB).

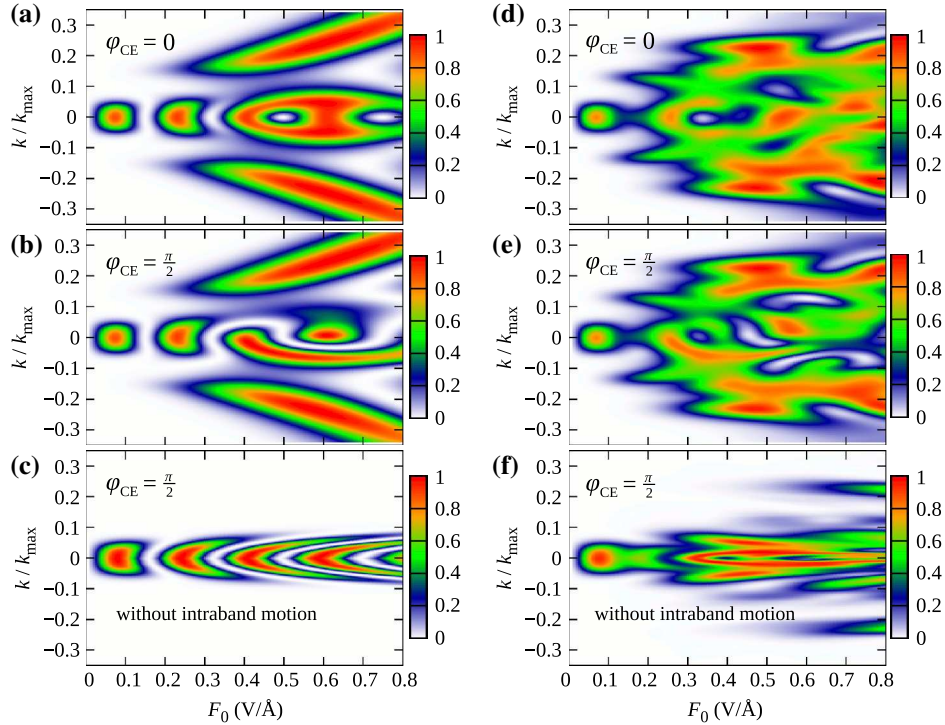


FIG. 3. The residual population of the lowest conduction band $n_{c_1}(k, t_{\max})$ in simulations with two (a)–(c) and six (d)–(f) bands without dephasing ($T_2 = \infty$). The CEP of the laser pulse is $\varphi_{\text{CE}} = 0$ in panels (a),(d) and $\pi/2$ in the other plots. Panels (c),(f) display population distributions obtained without intraband motion.

To gain more insight, we analyze in Fig. 3 the residual population $n_{c_1}(k, t_{\max})$ of the lowest conduction band (c_1). Higher bands contribute significantly less to the electric current. As we have already pointed out, dephasing with a typical rate of $T_2 \gtrsim 10$ fs has a minor effect; therefore, we set $T_2 = \infty$. We start with the case of two bands displayed in Figs. 3(a)–3(c) where it is easier to disentangle different processes. For $\varphi_{\text{CE}} = 0$ [panel (a)], the k -resolved population is symmetric, so that the residual intraband current is close to zero, in accord with Fig. 1. For $\varphi_{\text{CE}} = \pi/2$ [panel (b)], the residual conduction-band population becomes highly asymmetric in $\pm k$ in the region $F_0 \gtrsim 0.3$ V/Å and $|k|/k_{\max} \lesssim 0.1$. As Fig. 3(c) demonstrates, intraband motion plays a key role here. Eliminating it by dropping the term $\propto \mathbf{F}(t) \cdot \nabla_k \rho_{ij}$ in Eq. (1) leads to a fully symmetric distribution of excitation probabilities and also removes the carrier population at $k \gtrsim 0.2k_{\max}$.

Interband transitions predominantly occur in the part of the Brillouin zone where the corresponding transition matrix elements \mathbf{d}_{ij} have a large magnitude. For transitions from valence bands to the lowest conduction band of GaAs, $|\mathbf{d}_{ij}(\mathbf{k})|$ are maximal at the Γ point and sharply decrease for $k \gtrsim \Delta k = 0.1k_{\max}$ [23,37]. According to the Bloch acceleration theorem [38], an electron's crystal momentum in a given energy band, $\mathbf{K}(t)$, changes in time as $\mathbf{K}(t) = \mathbf{k} - e\hbar^{-1} \int_{t_0}^t \mathbf{F}(t') dt'$, where $\mathbf{k} = \mathbf{K}(t_0)$ is the initial momentum. At a characteristic field of $F \sim 0.4$ V/Å, an electron at the Γ point passes through the momentum range of interband

transitions during time $\tau \sim \hbar \Delta k / (eF_0) \sim 0.2$ fs. This time interval is much shorter than a half-cycle of both optical oscillations and Rabi oscillations.

Thus we predict a novel regime for solids in strong resonant optical fields where the population oscillations (which become Rabi oscillations in the limit of weaker and longer pulses) are excited by short and strong kicks during times when electrons pass the narrow crystal momentum region Δk near the Γ point. These kicks are repeated twice per optical cycle causing strongly anharmonic (nonsinusoidal in time) Rabi oscillations. We call this regime “kicked anharmonic Rabi oscillations” (KARO). It is illustrated in Fig. 4, where we show the time dependence of the lowest CB population for selected reciprocal-space pathways: $n_{c_1}[\mathbf{K}(t), t]$ undergoes very rapid changes at the moments of the kicks, and it is nearly constant between them. Such transitions can excite or deexcite electrons, and their overall outcome depends on the field amplitude and initial momentum \mathbf{k} , in turn defining whether there is a “bright” (high n_{c_1}) or “dark” (low n_{c_1}) fringe. At the Γ point ($k = 0$) in Fig. 4, the blue curve clearly indicates alternation of such excitation or deexcitation events. For $k \neq 0$ (the green curve), an electron passes near the Γ point at nonequidistant moments of time, which affects the final population and current.

If the intraband motion is artificially switched off, the fringes in Fig. 3(c) repeat periodically, as expected for Rabi oscillations, and the distribution is precisely symmetric: $n_{c_1}(k, t_{\max}) = n_{c_1}(-k, t_{\max})$. In contrast, the KARO regime in Figs. 3(a) and 3(b) manifests itself by the fringe spacing

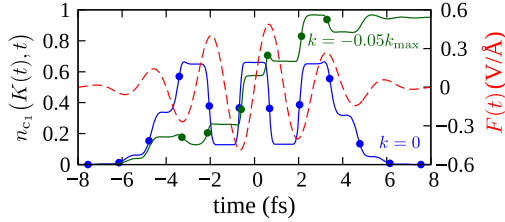


FIG. 4. Time dependence of the CB population in the two-band simulation (blue and green curves). It is calculated along reciprocal-space pathways $K(t)$ that satisfy the acceleration theorem. The starting point is the Γ point ($k = 0$) for the blue curve and $k = -0.05k_{\max}$ for the green curve. The bold dots on the curves denote moments of passage in the vicinity of the Γ point. The dashed red curve shows the electric field of the pulse ($F_0 = 0.5 \text{ V/\AA}$, $\varphi_{\text{CE}} = \pi/2$).

increasing with F_0 . However, the most important signature of the KARO is the evident asymmetry of the CB density distribution ($k < 0$ vs $k > 0$), which appears due to the intraband electron motion induced by an ultrashort pulse. The number of Rabi cycles increases with the field amplitude; when the pulse duration corresponds to an integer number of full oscillations, the residual current switches its direction—cf. Fig. 1. We interpret this switching of current as resulting from interference of electron pathways in reciprocal space.

The change of band populations between times t_i and t_f is determined by the field work, $W = \int_{t_i}^{t_f} \mathbf{F}(t) \mathbf{P}'(t) dt$, where $\mathbf{P}'(t)$ is the time derivative of the macroscopic polarization induced by both bound and free charges [39]. In the KARO process, the field changes little during a single kick. Consequently, a kick at time t does work $\Delta W \approx F(t) \Delta \mathbf{P}(t)$, where $\Delta \mathbf{P}$ is the corresponding polarization change. Two kicks that promote electrons from band j to band i at times t_1 and t_2 interfere with each other according to the phase accumulated by the interband polarization between the kicks. For a particular electron with initial crystal momentum \mathbf{k} , this phase is approximately given by (see Supplemental Material [23])

$$\Delta \phi_{ij}(\mathbf{k}) = \frac{1}{\hbar} \int_{t_1}^{t_2} dt \Delta E_{ij}(\mathbf{K}(t)). \quad (3)$$

It is analogous to the Volkov phase [40] in atomic physics. Let us consider two pathways separated by an optical cycle: $t_2 - t_1 = 2\pi/\omega_0$. When $\Delta \phi_{ij}(\mathbf{k}) = 2\pi q$, where integer q is the order of a nonlinear resonance, constructive interference results in net excitation of electrons.

In Figs. 3(a)–(b), it is evident that a region of strongly nonlinear behavior occurs at $F_0 \gtrsim 0.5 \text{ V/\AA}$. A nonlinear resonance of the lowest order ($q = 2$) for electron wave packets excited near the Γ point occurs for $\Delta \phi_{ij}(0) = 4\pi$. In a model with two parabolic bands, $\Delta E_{ij}(\mathbf{k}) \approx E_g + \hbar^2 k^2 / (2\mu)$, where μ is reduced effective mass. From Eq. (3), we obtain the second-order resonance

condition as $E_g + U_p = 2\hbar\omega_0$, where $U_p = e^2 F_0^2 / (4\mu\omega_0^2)$ is known as ponderomotive energy. Using $\mu = 0.05m_0$ for transitions from the light-hole VB to the lowest CB in GaAs, we estimate an onset of the resonance at $F_0 = 0.3 \text{ V/\AA}$. A more careful calculation that takes band nonparabolicity into account yields $F_0 = 0.5 \text{ V/\AA}$.

While we have concentrated above on a two-band model, real crystals contain a number of bands that can contribute to nonlinear optical phenomena in strong fields. Figures 3(d)–3(f) show that increasing the number of bands to six has a dramatic effect on the simulations for $F_0 \gtrsim 0.1 \text{ V/\AA}$: reciprocal-space populations are perturbed in a highly irregular, quasistochastic way; they become significantly asymmetric at lower laser fields, and signatures of Rabi cycles at $\mathbf{k} = 0$ are not as clearly visible even if intraband motion is neglected. Apparently, coherent effects suffer from effective dephasing induced by intraband motion in the presence of multiple bands. Similarly to Landau damping [41], this phenomenon is not related to electron-electron collisions or interaction with environment.

Our results also highlight the role of symmetries in strong-field phenomena. For $\varphi_{\text{CE}} = 0$, the Hamiltonian is symmetric with respect to time reversal. For $\varphi_{\text{CE}} = \pm\pi/2$, it is PT symmetric, that is, invariant under simultaneous parity (P) and time-reversal (T) transformations. The symmetries of final states match those of the Hamiltonian in two-band simulations (e.g., there is the $\mathbf{k} \leftrightarrow -\mathbf{k}$ symmetry for $\varphi_{\text{CE}} = 0$). Adding more bands breaks this apparent relation (see Figs. 1 and 3).

In conclusion, interaction of strong ultrashort laser pulses with a semiconductor is characterized by rapid passage of the efficient transition region (the vicinity of the Γ point), which brings about a new excitation regime that we call kicked anharmonic Rabi oscillations (KARO). This effect is due to quantum interference between kicklike transitions. Resonances that emerge from interfering kicks manifest themselves in highly asymmetric residual excitation distribution in reciprocal space and, consequently, a strong residual electric current. The predicted effects are experimentally observable: the asymmetric momentum distribution can be directly observed using angle-resolved photoemission spectroscopy (ARPES) [42–45], and the residual current can be detected through accompanying terahertz radiation [37,46,47]. Our findings add resonant processes to the toolkit of petahertz solid-state technology where potential applications may range from CEP detection [48] to sub-laser-cycle spectroscopy [49] and ultrafast signal processing [6].

We gratefully acknowledge F. Krausz for drawing our interest to resonant strong-field interactions and for his comments. M. S. W. was supported by the International Max Planck Research School of Advanced Photon Science. The work of M. S. W., S. Yu. K., and M. C. was supported by the DFG Cluster of Excellence: Munich-Centre for Advanced Photonics (MAP). The work of M. I. S. was

supported by the a MURI Grant No. FA9550-15-1-0037 from the U.S. Airforce Office of Scientific Research. A support for V. S. Y. came from a MURI Grant No. N00014-13-1-0649 from the U.S. Office of Naval Research.

* michael.wismer@mpq.mpg.de

† stanislav.kruchinin@mpq.mpg.de

* mstockman@gsu.edu

§ vyakovlev@gsu.edu

- [1] C. Zener, *Proc. R. Soc. A* **145**, 523 (1934).
- [2] L. V. Keldysh, *Sov. Phys. JETP* **20**, 1307 (1965).
- [3] S. Ghimire, A. D. DiChiara, E. Sistrunk, P. Agostini, L. F. DiMauro, and D. A. Reis, *Nat. Phys.* **7**, 138 (2011).
- [4] A. Schiffrin, T. Paasch-Colberg, N. Karpowicz, V. Apalkov, D. Gerster, S. Muehlbrandt, M. Korbman, J. Reichert, M. Schultz, S. Holzner, J. V. Barth, R. Kienberger, R. Ernstorfer, V. S. Yakovlev, M. I. Stockman, and F. Krausz, *Nature (London)* **493**, 70 (2013).
- [5] M. Schultze, E. M. Bothschafter, A. Sommer, S. Holzner, W. Schweinberger, M. Fiess, M. Hofstetter, R. Kienberger, V. Apalkov, V. S. Yakovlev, M. I. Stockman, and F. Krausz, *Nature (London)* **493**, 75 (2013).
- [6] F. Krausz and M. I. Stockman, *Nat. Photonics* **8**, 205 (2014).
- [7] M. Schultze, K. Ramasesha, C. D. Pemmaraju, S. A. Sato, D. Whitmore, A. Gandman, J. S. Prell, L. J. Borja, D. Prendergast, K. Yabana, D. M. Neumark, and S. R. Leone, *Science* **346**, 1348 (2014).
- [8] O. Schubert, M. Hohenleutner, F. Langer, B. Urbanek, C. Lange, U. Huttner, D. Golde, T. Meier, M. Kira, S. W. Koch, and R. Huber, *Nat. Photonics* **8**, 119 (2014).
- [9] T. T. Luu, M. Garg, S. Yu. Kruchinin, A. Moulet, M. Th. Hassan, and E. Goulielmakis, *Nature (London)* **521**, 498 (2015).
- [10] G. Vampa, T. J. Hammond, N. Thiré, B. E. Schmidt, F. Légaré, C. R. McDonald, T. Brabec, and P. B. Corkum, *Nature (London)* **522**, 462 (2015).
- [11] M. Hohenleutner, F. Langer, O. Schubert, M. Knorr, U. Huttner, S. W. Koch, M. Kira, and R. Huber, *Nature (London)* **523**, 572 (2015).
- [12] G. Vampa, T. J. Hammond, N. Thiré, B. E. Schmidt, F. Légaré, C. R. McDonald, T. Brabec, D. D. Klug, and P. B. Corkum, *Phys. Rev. Lett.* **115**, 193603 (2015).
- [13] D. J. Jones, S. A. Diddams, J. K. Ranka, A. Stentz, R. S. Windeler, J. L. Hall, and S. T. Cundiff, *Science* **288**, 635 (2000).
- [14] S. Hughes, *Phys. Rev. Lett.* **81**, 3363 (1998).
- [15] O. D. Mücke, T. Tritschler, M. Wegener, U. Morgner, and F. X. Kärtner, *Phys. Rev. Lett.* **87**, 057401 (2001).
- [16] O. D. Mücke, T. Tritschler, M. Wegener, U. Morgner, and F. X. Kärtner, *Phys. Rev. Lett.* **89**, 127401 (2002).
- [17] O. D. Mücke, T. Tritschler, M. Wegener, U. Morgner, F. X. Kärtner, G. Khitrova, and H. M. Gibbs, *Opt. Lett.* **29**, 2160 (2004).
- [18] R. Atanasov, A. Haché, J. L. P. Hughes, H. M. van Driel, and J. E. Sipe, *Phys. Rev. Lett.* **76**, 1703 (1996).
- [19] T. M. Fortier, P. A. Roos, D. J. Jones, S. T. Cundiff, R. D. R. Bhat, and J. E. Sipe, *Phys. Rev. Lett.* **92**, 147403 (2004).
- [20] D. Golde, T. Meier, and S. W. Koch, *Phys. Rev. B* **77**, 075330 (2008).
- [21] P. Blaha, K. Schwarz, G. K. H. Madsen, D. Kvasnicka, and J. Luitz, *WIEN2K, An Augmented Plane Wave+Local Orbitals Program for Calculating Crystal Properties* (Karlheinz Schwarz, Techn. Universität Wien, Austria, 2001).
- [22] X. Zhang, Y. Jin, and X. F. Ma, *Appl. Phys. Lett.* **61**, 2764 (1992).
- [23] See Supplemental Material at <http://link.aps.org/supplemental/10.1103/PhysRevLett.116.197401>, which includes Refs. [24–32], for details of the model and additional results supporting our main conclusions.
- [24] F. Tran and P. Blaha, *Phys. Rev. Lett.* **102**, 226401 (2009).
- [25] J. Blakemore, *J. Appl. Phys.* **53**, R123 (1982).
- [26] Yu. A. Bychkov and A. M. Dykhne, *Sov. Phys. JETP* **31**, 928 (1970).
- [27] J. B. Krieger and G. J. Iafrate, *Phys. Rev. B* **33**, 5494 (1986).
- [28] S. Yu. Kruchinin, M. Korbman, and V. S. Yakovlev, *Phys. Rev. B* **87**, 115201 (2013).
- [29] L. Huang, J. P. Callan, E. N. Glezer, and E. Mazur, *Phys. Rev. Lett.* **80**, 185 (1998).
- [30] L. Hedin, *Phys. Rev.* **139**, A796 (1965).
- [31] M. S. Hybertsen and S. G. Louie, *Phys. Rev. B* **34**, 5390 (1986).
- [32] F. Aryasetiawan and O. Gunnarsson, *Rep. Prog. Phys.* **61**, 237 (1998).
- [33] S. S. Prabhu, S. E. Ralph, M. R. Melloch, and E. S. Harmon, *Appl. Phys. Lett.* **70**, 2419 (1997).
- [34] S. Funk, G. Acuna, M. Handloser, and R. Kersting, *Opt. Express* **17**, 17450 (2009).
- [35] P. C. Becker, H. L. Fragnito, C. H. Brito Cruz, R. L. Fork, J. E. Cunningham, J. E. Henry, and C. V. Shank, *Phys. Rev. Lett.* **61**, 1647 (1988).
- [36] Q. T. Vu, H. Haug, O. D. Mücke, T. Tritschler, M. Wegener, G. Khitrova, and H. M. Gibbs, *Phys. Rev. Lett.* **92**, 217403 (2004).
- [37] W. Kuehn, P. Gaal, K. Reimann, M. Woerner, T. Elsaesser, and R. Hey, *Phys. Rev. B* **82**, 075204 (2010).
- [38] F. Bloch, *Z. Phys.* **52**, 555 (1929).
- [39] L. D. Landau and E. M. Lifshitz, *Electrodynamics of Continuous Media* (Pergamon, Oxford and New York, 1984).
- [40] D. M. Wolkow, *Zeitschrift für Physik* **94**, 250 (1935).
- [41] L. D. Landau, *J. Phys. (USSR)* **10**, 25 (1946). *Collected Papers of L. D. Landau*, edited by D. Ter Haar (Pergamon Press Ltd. and Gordon and Breach, Science Publishers, 1965).
- [42] A. Damascelli, Z. Hussain, and Z. X. Shen, *Rev. Mod. Phys.* **75**, 473 (2003).
- [43] S. Mathias, L. Miaja-Avila, M. M. Murnane, H. Kapteyn, M. Aeschlimann, and M. Bauer, *Rev. Sci. Instrum.* **78**, 083105 (2007).
- [44] J. Güdde, M. Rohleder, T. Meier, S. W. Koch, and U. Höfer, *Science* **318**, 1287 (2007).
- [45] W. S. Lee, I. M. Vishik, D. H. Lu, and Z. X. Shen, *J. Phys. Condens. Matter* **21**, 164217 (2009).
- [46] D. Côté, J. M. Fraser, M. DeCamp, P. H. Bucksbaum, and H. M. van Driel, *Appl. Phys. Lett.* **75**, 3959 (1999).
- [47] M. Spasenović, M. Betz, L. Costa, and H. M. van Driel, *Phys. Rev. B* **77**, 085201 (2008).
- [48] T. Paasch-Colberg, A. Schiffrin, N. Karpowicz, S. Kruchinin, Ö. Sağlam, S. Keiber, O. Razskazovskaya, S. Muehlbrandt, A. Alnaser, M. Kübel, V. Apalkov, D. Gerster, J. Reichert, T. Wittmann, J. V. Barth, M. I. Stockman, R. Ernstorfer, V. S. Yakovlev, R. Kienberger, and F. Krausz, *Nat. Photonics* **8**, 214 (2014).
- [49] M. Ivanov and O. Smirnova, *Chem. Phys.* **414**, 3 (2013).

Supplemental Material to “Strong-field resonant dynamics in semiconductors”

Michael S. Wismer,^{1,*} Stanislav Yu. Kruchinin,^{1,†} Marcelo Ciappina,¹ Mark I. Stockman,^{2,‡} and Vladislav S. Yakovlev^{1,2,§}

¹Max-Planck-Institut für Quantenoptik, Hans-Kopfermann-Str. 1, 85748 Garching, Germany

²Center for Nano-Optics (CeNO) and Department of Physics and Astronomy,

Georgia State University, Atlanta, Georgia 30340, USA

(Dated: March 1, 2016)

I. BAND STRUCTURE CALCULATIONS

Fig. S1 shows the band energies and matrix elements of GaAs that we obtained from the density functional theory (DFT) calculations, where we used the TB09 meta-GGA exchange-correlation potential¹ with spin-orbit coupling. The calculated band-gap energy is $E_g = 1.55$ eV, which is somewhat larger than the measured band gap at room temperature (1.42 eV) but close to that at low temperatures (1.52 eV)².

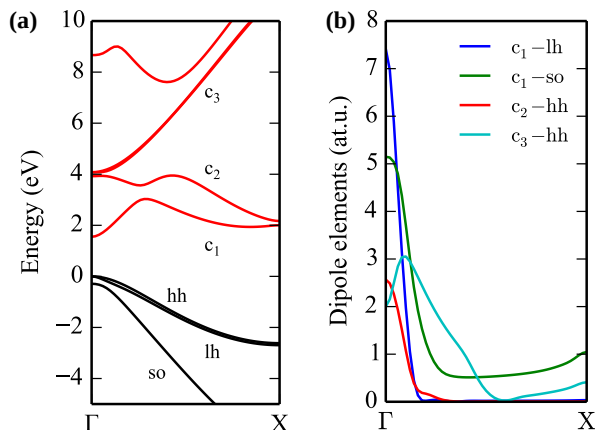


FIG. S1. (a) The energies of three highest valence bands (black) and five lowest conduction bands (red) of GaAs along the line between the Γ and X points. Each of these bands is doubly degenerate. (b) Dipole moments $|\mathbf{d}_{ij}(\mathbf{k})|$ for the most important interband transitions.

We evaluate the reduced electron mass by fitting the gap between the lowest conduction band (c_1) and the light-hole (lh) band with a second-order polynomial within $|\mathbf{k}| \leq 0.05k_{\max}$. The result is $0.053m_0$.

The Wien2K code only provides us with momentum matrix elements \mathbf{p}_{ij} , so we evaluated the interband matrix elements of crystal coordinate via $\mathbf{d}_{i \neq j}(\mathbf{k}) = i\hbar\mathbf{p}_{ij}(\mathbf{k}) / (m_0[E_i(\mathbf{k}) - E_j(\mathbf{k})])$, where m_0 is the free electron mass. We found that Berry connections $e^{-1}\mathbf{d}_{ii}$ had a negligible effect on the residual intraband current density, so we assumed $\mathbf{d}_{ii} = 0$.

II. EXTERNAL FIELD

Fig. S2(a) shows the field $F(t)$ that we used in our simulations, while Fig. S2(b) shows the power spectrum of the pulse. We define the field $F(t) = \hat{\mathbf{e}}\mathbf{F}(t)$ in the

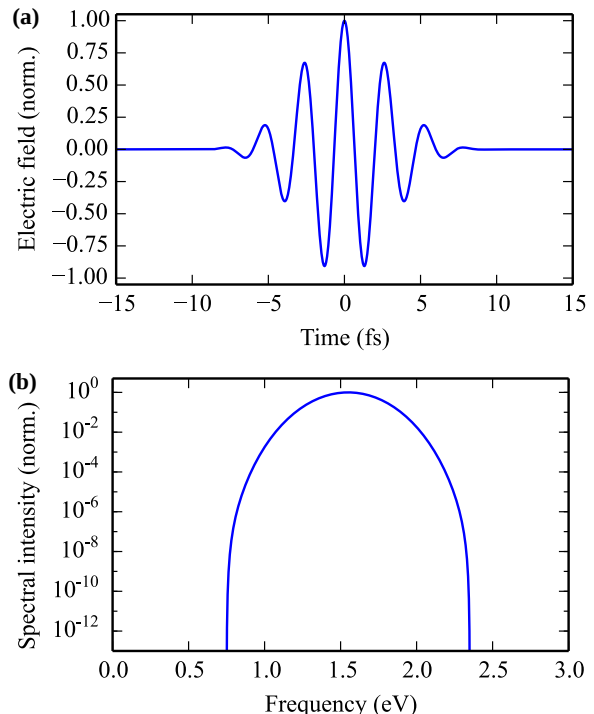


FIG. S2. (a) Normalized electric field inside the medium. (b) The power spectrum of the laser pulse in the limit of an infinitely broad temporal window.

frequency domain taking the spectrum $\tilde{F}(\omega)$ as a Nuttall window centered at $\omega_0 = \hbar^{-1}E_g$ with a compact support in the interval $E_g - \hbar\Delta\omega \leq \hbar\omega \leq E_g + \hbar\Delta\omega$ with $\hbar\Delta\omega = 0.8$ eV. The central wavelength of the pulse is $\lambda_0 = 2\pi c/\omega_0 = 800$ nm; its central photon energy is $\hbar\omega_0 = E_g = 1.55$ eV. In the time domain, the intensity of the pulse has a full width at half maximum (FWHM) of 5 fs; our simulations begin at $t_0 = -36.2$ and end at $t_{\max} = 36.2$ fs. An explicit expression for the positive-frequency part of the pulse spectrum is $\tilde{F}(\omega) = \tilde{F}_0 \exp(i\varphi_{\text{CE}})w[(\omega - \omega_0 + \Delta\omega)/(2\Delta\omega)]$, where φ_{CE} is the carrier-envelope phase. The Nuttall window is defined as $w(x) = \sum_{n=0}^3 a_n \cos(2\pi nx)$ if $0 \leq x \leq 1$

and $w(x) = 0$ outside of this interval. The coefficients are $a_0 = 0.355768$, $a_1 = -0.487396$, $a_2 = 1/2 - a_0$, and $a_3 = -(1/2 + a_1)$.

III. TEMPORAL EVOLUTION

Fig. S3 illustrates the temporal evolution of electronic excitations in two-band simulations. Interband transitions mainly take place near the Γ point. Electron-hole wavepackets excited by different laser half-cycles interfere with each other. This interference determines residual reciprocal-space population distributions. Asymmetric distributions yield residual ballistic electric current.

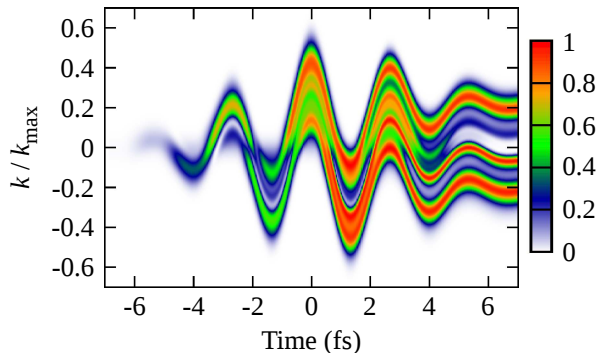


FIG. S3. Temporal evolution of the conduction-band population in a two-band simulation for $F_0 = 0.5$ V/Å, $\varphi_{CE} = \pi/2$, $T_2 = \infty$.

Fig. S4 is analogous to Fig. 4 in the main text, but it represents results obtained in a six-band simulation. Temporally confined transitions between valence and conduction bands are still clearly visible, but the presence of multiple bands makes the dynamics more complicated.

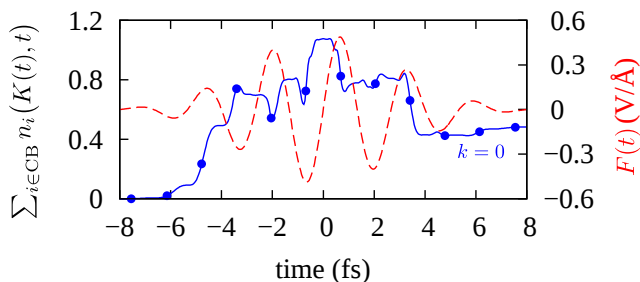


FIG. S4. Time dependence of the total CB population in a six-band simulation (blue curve). It is calculated along the reciprocal-space pathway $K(t)$ that satisfies the acceleration theorem and begins at the Γ point ($k = 0$). The bold dots denote moments of passage of the reciprocal-space trajectory through the Γ point. The dashed red curve shows the electric field of the pulse ($F_0 = 0.5$ V/Å, $\varphi_{CE} = \pi/2$).

IV. QUANTUM-PATH INTERFERENCE IN RECIPROCAL SPACE

As explained in the main text, the KARO regime is characterized by “kick-like” interband transitions that take place when an electron moving along a reciprocal-space trajectory,

$$\mathbf{K}(t) = \mathbf{k} - \frac{e}{\hbar} \int_{t_0}^t \mathbf{F}(t') dt', \quad (1)$$

traverses a region where the corresponding transition matrix element $\mathbf{d}_{ij}(\mathbf{K}(t))$ is particularly large. In this section, we study how such temporally confined transitions interfere with each other. This task is most easily accomplished if we neglect interband phase relaxation ($T_2 \rightarrow \infty$) and solve the time-dependent Schrödinger equation in the basis of Houston states. Let $|\psi_i(\mathbf{k})\rangle$ be a Bloch state for band i and crystal momentum \mathbf{k} . Using the ansatz

$$|\Psi_{\mathbf{k}}(t)\rangle = \sum_i \alpha_{i,\mathbf{k}}(t) e^{-\frac{i}{\hbar} \int_{t_0}^t dt' E_i(\mathbf{K}(t'))} |\psi_i(\mathbf{K}(t))\rangle, \quad (2)$$

where $\alpha_{i,\mathbf{k}}(t)$ are probability amplitudes, we obtain the following equations^{3,4}:

$$\frac{d}{dt} \alpha_{i,\mathbf{k}}(t) = -\frac{i}{\hbar} \sum_j \alpha_{j,\mathbf{k}}(t) \mathbf{F}(t) \cdot \mathbf{d}_{ij}(\mathbf{K}(t)) \times \exp\left[\frac{i}{\hbar} \int_{t_0}^t dt' \Delta E_{ij}(\mathbf{K}(t'))\right]. \quad (3)$$

Ansatz (2) accounts for the intraband motion, as well as for the quantum phase accumulated by a wave function in the absence of interband transitions. Therefore, probability amplitudes $\alpha_{i,\mathbf{k}}(t)$ only change their values when electrons are excited or de-excited. Now we introduce the approximation of sudden transitions at a series of moments $\{t_n\}$, which may themselves depend on initial crystal momentum \mathbf{k} :

$$\mathbf{d}_{ij}(\mathbf{K}(t)) \approx \sum_n \delta(t - t_n) \int_{t_n - \Delta t}^{t_n + \Delta t} dt \mathbf{d}_{ij}(\mathbf{K}(t)). \quad (4)$$

Here, $\delta(t)$ is the Dirac delta-function, $|\mathbf{d}_{ij}(\mathbf{K}(t))|$ has a local maximum at $t = t_n$, and the integration is performed over a short interval of time ($\Delta t \ll t_{n+1} - t_n$) during which transitions are most probable. Let us change the integration variable from time to crystal momentum assuming that the laser field is linearly polarized along a unit vector $\hat{\mathbf{e}}$:

$$\int_{t_n - \Delta t}^{t_n + \Delta t} dt \mathbf{d}_{ij}(\mathbf{K}(t)) = \int_{\mathbf{K}(t_n - \Delta t)}^{\mathbf{K}(t_n + \Delta t)} \frac{dk}{|\mathbf{K}'(t)|} \mathbf{d}_{ij}(\mathbf{k}) \approx -\frac{\hbar}{e|F(t_n)|} \int_{-\Delta k}^{\Delta k} dk \mathbf{d}_{ij}(\mathbf{K}(t_n) + k\hat{\mathbf{e}}). \quad (5)$$

Here, $\Delta k = e\hbar^{-1}|F_0| \sim |\mathbf{K}'(t_n)| \Delta t$. Introducing

$$D_{ij}(\mathbf{k}, t_n) = \frac{1}{e} \int_{-\Delta k}^{\Delta k} dk \mathbf{d}_{ij}(\mathbf{K}(t_n) + k\hat{\mathbf{e}}), \quad (6)$$

we re-write Eq. (3) as

$$\begin{aligned} \frac{d}{dt} \alpha_{i,\mathbf{k}}(t) &\approx i \sum_j \alpha_{j,\mathbf{k}}(t) \exp \left[\frac{i}{\hbar} \int_{t_0}^t dt' \Delta E_{ij}(\mathbf{K}(t')) \right] \\ &\times \sum_n \delta(t - t_n) \text{sgn}[F(t_n)] D_{ij}(\mathbf{k}, t_n). \end{aligned} \quad (7)$$

In this model, the probability amplitudes stay constant between kicks, and they change their values abruptly at each kick. A general solution of Eq. (7) can be written in the matrix form. For one particular transition at time t_n ,

$$\boldsymbol{\alpha}_{\mathbf{k}}(t_n + \Delta t) = e^{i\hat{M}(\mathbf{k}, t_n)} \boldsymbol{\alpha}_{\mathbf{k}}(t_n - \Delta t), \quad (8)$$

where the elements of matrix $\hat{M}(\mathbf{k}, t_n)$ are given by

$$\begin{aligned} M_{ij}(\mathbf{k}, t_n) &= \exp \left[\frac{i}{\hbar} \int_{t_0}^{t_n} dt' \Delta E_{ij}(\mathbf{K}(t')) \right] \\ &\times \text{sgn}[F(t_n)] D_{ij}(\mathbf{k}, t_n). \end{aligned} \quad (9)$$

As long as the probability of a particular transition is small, then $e^{i\hat{M}(\mathbf{k}, t_n)} \approx 1 + i\hat{M}(\mathbf{k}, t_n)$. In this approximation,

$$\begin{aligned} \Delta \alpha_{i,\mathbf{k}}(t_n) &= \alpha_{i,\mathbf{k}}(t_n + \Delta t) - \alpha_{i,\mathbf{k}}(t_n - \Delta t) \approx \\ &i \text{sgn}[F(t_n)] \sum_j \left\{ \alpha_{j,\mathbf{k}}(t_n - \Delta t) D_{ij}(\mathbf{k}, t_n) \right. \\ &\left. \times \exp \left[\frac{i}{\hbar} \int_{t_0}^{t_n} dt' \Delta E_{ij}(\mathbf{K}(t')) \right] \right\}. \end{aligned} \quad (10)$$

Whether two particular excitation events at times t_{n_1} and t_{n_2} interfere constructively or destructively depends on the relative phase between $\Delta \alpha_{i,\mathbf{k}}(t_{n_1})$ and $\Delta \alpha_{i,\mathbf{k}}(t_{n_2})$, which is given by $\Delta \phi(\mathbf{k}) = \arg \left[\Delta \alpha_{i,\mathbf{k}}^*(t_{n_1}) \Delta \alpha_{i,\mathbf{k}}(t_{n_2}) \right]$. If we constraint ourselves to transitions from band j to band $i \neq j$, then Eq. (10) yields

$$\begin{aligned} \Delta \phi_{ij}(\mathbf{k}) &= \arg \left\{ \text{sgn}[F(t_{n_1})F(t_{n_2})] \times \right. \\ &\alpha_{j,\mathbf{k}}^*(t_{n_1} - \Delta t) \alpha_{j,\mathbf{k}}(t_{n_2} - \Delta t) D_{ij}^*(\mathbf{k}, t_{n_1}) D_{ij}(\mathbf{k}, t_{n_2}) \\ &\left. \times \exp \left[\frac{i}{\hbar} \int_{t_0}^{t_{n_2}} dt' \Delta E_{ij}(\mathbf{K}(t')) \right] \right\}. \end{aligned} \quad (11)$$

If both transitions take place at the same \mathbf{k} (e.g. $\mathbf{k} = 0$), then $D_{ij}(\mathbf{k}, t_{n_1}) = D_{ij}(\mathbf{k}, t_{n_2})$. Since we are currently considering small transition probabilities, we can neglect the change of phase of the initial state: $\arg[\alpha_{j,\mathbf{k}}^*(t_{n_1} -$

$\Delta t) \alpha_{j,\mathbf{k}}(t_{n_2} - \Delta t)]$. These considerations lead us to the following result:

$$\begin{aligned} \Delta \phi_{ij}(\mathbf{k}) &\approx \frac{\pi}{2} \left(1 - \text{sgn}[F(t_{n_1})F(t_{n_2})] \right) \\ &+ \frac{1}{\hbar} \int_{t_{n_1}}^{t_{n_2}} dt' \Delta E_{ij}(\mathbf{K}(t')). \end{aligned} \quad (12)$$

The first term on the right-hand side of this equation disappears if t_{n_1} and t_{n_2} are separated by a full laser cycle, and it is equal to π if the laser field changes its sign between these two moments of time.

V. RABI FLOPPING

As an attempt to disentangle intraband motion from Rabi oscillations, we repeat our simulations with all the transition matrix elements reduced by a factor of 10. In the absence of detuning, this would decrease the Rabi frequency by the same factor. Intraband motion causes a large time-dependent detuning enabling interference effects that strongly resemble Rabi flopping, as one can see in Fig. S5. There are indeed no signatures of Rabi oscillations if there is no intraband motion [panel (c)]; however, in panels (a) and (b), we see periodic local minima or the conduction-band population at $k = 0$. The field strengths at which these minima occur are slightly larger than those in Fig. 3 of the main text. Similarly to Fig. 3, strongly asymmetric distributions form at $F_0 \gtrsim 0.4 \text{ V/\AA}$.

To verify that the periodic destructive interference at $k = 0$ can be related to Rabi oscillations, we evaluate the pulse area, accounting for the time-dependent detuning induced by the intraband motion:

$$\mathcal{A} = \int_{-\infty}^{\infty} dt \sqrt{|\Omega_R(t)|^2 + [\Delta E_{ij}(K(t)) - \hbar\omega_0]^2}, \quad (13a)$$

$$\Omega_R(t) = \frac{d_{ij}(K(t))f(t)}{\hbar}, \quad (13b)$$

$$K(t) = \frac{e}{\hbar} A(t). \quad (13c)$$

Here, $f(t)$ is the envelope of the electric field:

$$F(t) = 2 \text{Re} [f(t)e^{-i\omega_0 t}]. \quad (14)$$

A long laser pulse with a constant detuning completes an integer number of Rabi cycles if its pulse area is equal to an integer multiple of 2π . Even though we consider a few-cycle pulse where detuning $\Delta E(K(t)) - \hbar\omega_0$ significantly changes within a fraction of a cycle, it is still instructive to evaluate the pulse amplitudes that satisfy $\mathcal{A} = 2\pi n$ ($n \in \mathbb{N}$). These field strengths are indicated in Fig. S5 by red crosses, the corresponding values being 0.26, 0.43, and 0.61 V/\AA. The same analysis applied to the original matrix elements yields peak field strengths of 0.16, 0.33, and 0.48 V/\AA, which agree well with the results shown in Fig. 3 of the main text. Therefore, in

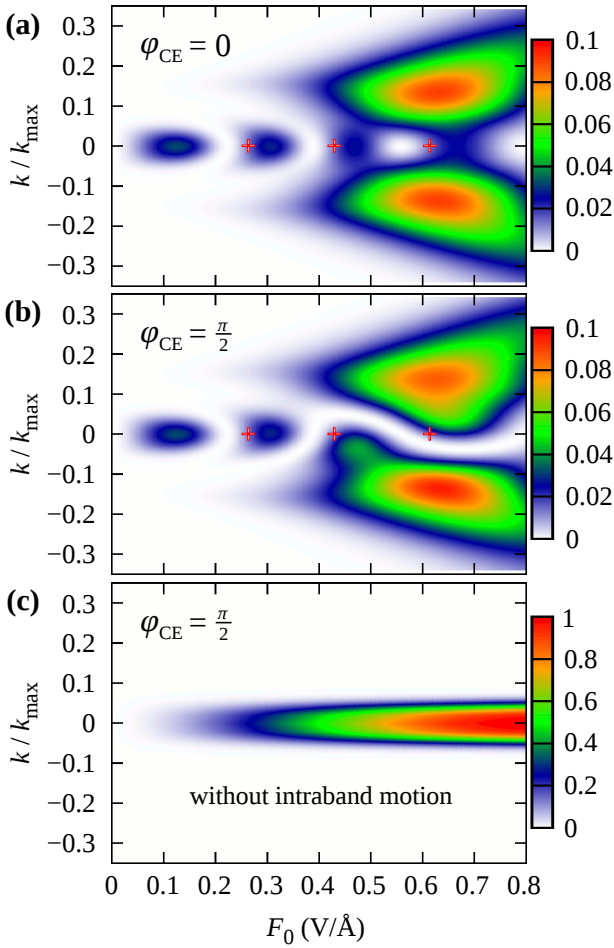


FIG. S5. The same as Fig. 3 of the main text, but all the transition matrix elements were reduced by a factor of 10 in order to suppress Rabi oscillations. The false colors represent the residual population of conduction-band states in the two-band simulations without dephasing. The red crosses indicate the peak field strengths where the pulse area \mathcal{A} [see Eqs. (13)] is an integer multiple of 2π . Due to reduced excitation probabilities, panels (a) and (b) use a different color scale.

these two examples (Figs. S5 and 3), kicked Rabi oscillations may also be interpreted as strongly detuned Rabi flopping. However, we do not know if Eq. (13a) is generally applicable in the KARO regime. Also, unlike the analysis presented in the previous section, Eqs. (13) is inapplicable to very broadband pulses where the central frequency is not well-defined and, therefore, Eq. (14) does not provide an unambiguous definition of pulse envelope.

Figure S6 shows that completing a Rabi cycle causes current reversal even when the transition matrix elements are reduced.

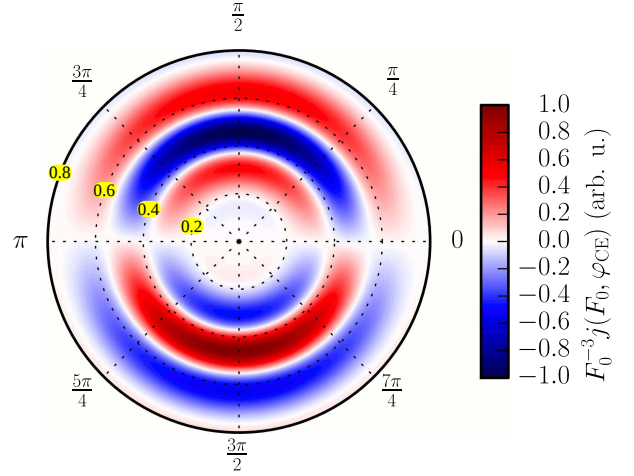


FIG. S6. Residual electric current evaluated with the transition matrix elements being reduced by a factor of 10. Here, we used two bands and $T_2 = \infty$.

VI. TRANSFERRED CHARGE

In this paper, we focused on the residual current density because this quantity is directly related to asymmetry in the residual band population, and also because it was primarily used in the previous work on $\omega + 2\omega$ interference. However, for an experimental verification of these results, the transferred charge may be a more relevant observable⁵⁻⁷. Fig. S7 is similar to Fig. 1 of the main text, but, instead of the residual current, we visualize the transferred charge density

$$Q(F_0, \varphi_{\text{CE}}) = \int_{-\infty}^{t_{\text{cut}}} dt j(F_0, \varphi_{\text{CE}}, t), \quad (15)$$

where we set the upper integration limit to $t_{\text{cut}} = 8$ fs and evaluate the time-dependent intraband current density according to

$$j(F_0, \varphi_{\text{CE}}, t) = -\frac{2e}{(2\pi)^3} \sum_i \int_{\text{BZ}} d^3k n_i(\mathbf{k}, t) \hat{\mathbf{e}}v_i(\mathbf{k}). \quad (16)$$

VII. ELECTRONIC EXCITATIONS

Figure S8 shows the residual excitation probability averaged along the Γ -X direction:

$$\bar{p}_{1\text{D}} = \frac{1}{2k_{\text{max}}} \int_{-k_{\text{max}}}^{k_{\text{max}}} p(k) dk.$$

Modulations of the population are most clearly seen for calculations involving two bands and $T_2 = \infty$. Increasing the number of bands and using a dephasing time of $T_2 = 10$ fs reduces the depth of the excitation minima.

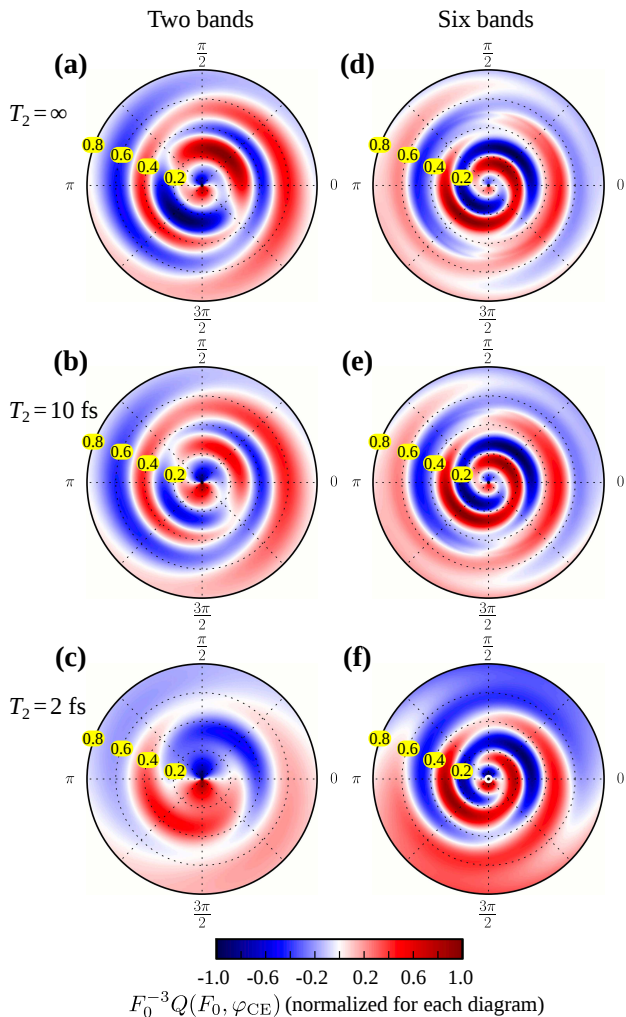


FIG. S7. The transferred charge density $Q(F_0, \varphi_{\text{CE}})$. In these diagrams, the distance to the origin corresponds to pulse amplitude F_0 , which varies from zero to 0.8 V/\AA , while the angle to the horizontal axis encodes the carrier-envelope phase φ_{CE} . The false colors represent $F_0^{-3}Q(F_0, \varphi_{\text{CE}})$ individually normalized for each diagram. The left three panels show two-band results (1 CB, 1 VB), while panels (d)-(f) show six-band results (3 CBs, 3 VBs). Each horizontal pair of plots corresponds to a certain value of the dephasing time T_2 as indicated by the labels.

We can roughly estimate 3D excitation probabilities by noticing that most transition matrix elements from valence bands to the lowest conduction band are insignificant for $|\mathbf{k}| \gtrsim 0.2k_{\text{max}} = k_0$ [see Fig. S1(b)]. In the KARO regime, electrons are efficiently excited within a cylinder in reciprocal space that is aligned with the laser polarization and has an effective radius of k_0 . Within this cylinder, we approximate the excitation profile as independent of the distance to the symmetry axis. Consequently, we estimate the excitation probability averaged over the Brillouin zone as

$$\bar{p}_{3\text{D}} \sim \frac{2k_{\text{max}}\pi k_0^2}{\Omega_{\text{BZ}}} \bar{p}_{1\text{D}} = \frac{(ak_0)^2}{8\pi} \bar{p}_{1\text{D}},$$

where $a = 5.65 \text{ \AA}$ is the lattice constant, and $\Omega_{\text{BZ}} = (2\pi)^3/(a^3/4)$ is the Brillouin-zone volume of GaAs. Taking the spin degeneracy into account, we estimate the concentration of charge carriers after the laser pulse to be $n_e \sim 2\bar{p}_{3\text{D}}/((a^3/4)) \approx 10^{21} \text{ cm}^{-3}$ at a field strength of $F_0 = 0.8 \text{ V/\AA}$. This is below the free-carrier density of 10^{22} cm^{-3} , which is expected to mark the damage threshold⁸.

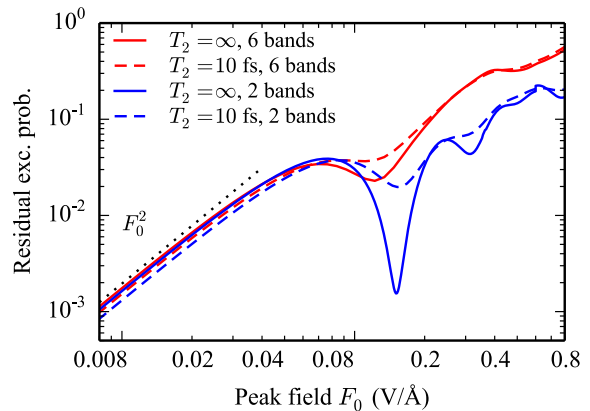


FIG. S8. Residual excitation probability $\bar{p}_{1\text{D}}$ as a function of the peak field.

VIII. EFFECT OF HIGHER CONDUCTION BANDS

Figures S9 and S10 illustrate that increasing the number of conduction bands from three to six in our model gives similar reciprocal-space distributions and residual current.

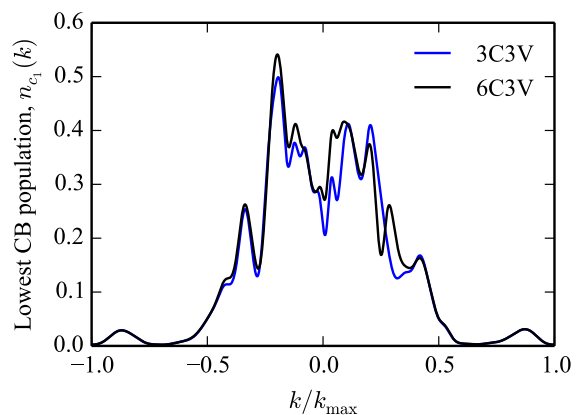


FIG. S9. The residual population of the lowest conduction band $n_{c_1}(k, t_{\text{max}})$ evaluated for $F_0 = 0.8 \text{ V/\AA}$ and $T_2 = 10 \text{ fs}$. The blue curve represents six-band simulations (3 CBs, 3 VBs). The black curve represents nine-band simulations (6 CBs, 3 VBs).

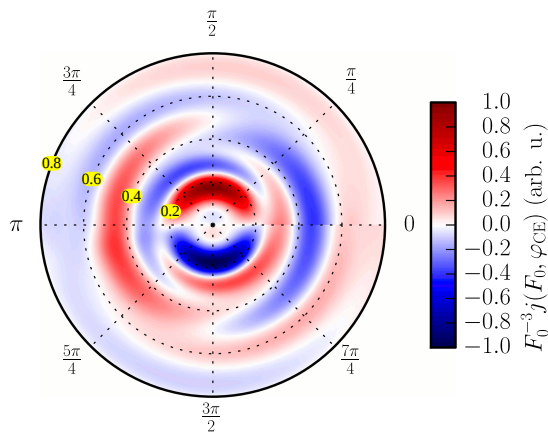


FIG. S10. The same as Fig. 1(e) of the main text, but evaluated with nine bands (6 CBs, 3 VBs). The plot shows the residual current density $j(F_0, \varphi_{CE})$ evaluated for $T_2 = 10$ fs.

As an important comment, we mention here that increasing the number of bands in computations based on Kohn-Sham DFT orbitals would not necessarily increase the veracity and precision of the corresponding results as the Kohn-Sham orbitals are not the actual quasiparticle states. In principle, one could evaluate the quasiparticle states using a more sophisticated and realistic GW method^{9–11}. However, the electron self-energy in this method possesses a nonzero imaginary part that is inversely proportional to the quasiparticle lifetime. The lifetime decreases rapidly for highly excited bands. Because of this, a single-particle description of electron dynamics in highly excited bands may be inadequate. We chose six-band (3C3V) calculations for the main text as a reasonable compromise that allows us to discuss general effects related to the inclusion of higher bands.

* michael.wismer@mpq.mpg.de

† stanislav.kruchinin@mpq.mpg.de

‡ mstockman@gsu.edu

§ vladislav.yakovlev@mpq.mpg.de

¹ F. Tran and P. Blaha, *Phys. Rev. Lett.* **102**, 226401 (2009).

² J. Blakemore, *J. Appl. Phys.* **53**, R123 (1982).

³ Y. A. Bychkov and A. M. Dykhne, *Sov. Phys. JETP* **31**, 928 (1970).

⁴ J. B. Krieger and G. J. Iafrate, *Phys. Rev. B* **33**, 5494 (1986).

⁵ A. Schiffrin, T. Paasch-Colberg, N. Karpowicz, V. Apalkov, D. Gerster, S. Muehlbrandt, M. Korbman, J. Reichert, M. Schultze, S. Holzner, J. V. Barth, R. Kienberger, R. Ernstorfer, V. S. Yakovlev, M. I. Stockman, and F. Krausz, *Nature* **493**, 70 (2013).

⁶ S. Yu. Kruchinin, M. Korbman, and V. S. Yakovlev, *Phys.*

Rev. B **87**, 115201 (2013).

⁷ T. Paasch-Colberg, A. Schiffrin, N. Karpowicz, S. Kruchinin, Ö. Sağlam, S. Keiber, O. Razskazovskaya, S. Mühlbrandt, A. Alnaser, M. Kübel, V. Apalkov, D. Gerster, J. Reichert, T. Wittmann, J. V. Barth, M. I. Stockman, R. Ernstorfer, V. S. Yakovlev, R. Kienberger, and F. Krausz, *Nature Photon.* **8**, 214 (2014).

⁸ L. Huang, J. P. Callan, E. N. Glezer, and E. Mazur, *Phys. Rev. Lett.* **80**, 185 (1998).

⁹ L. Hedin, *Phys. Rev.* **139**, A796 (1965).

¹⁰ M. S. Hybertsen and S. G. Louie, *Phys. Rev. B* **34**, 5390 (1986).

¹¹ F. Aryasetiawan and O. Gunnarsson, *Rep. Progr. Phys.* **61**, 237 (1998).